nature research

https://doi.org/10.1038/s41563-020-00859-3

Supplementary information

n-type charge transport in heavily p-doped polymers

In the format provided by the authors and unedited

Supplemental Information for:
_n_-Type Charge Transport in Heavily _p_-Doped Polymers

Zhiming Liang,[a] Hyun Ho Choi,[b] Xuyi Luo,[c] Tuo Liu,[a] Ashkan Abtahi,[a,d] Uma Shantini Ramasamy,[a,e] J. Andrew Hitron,[f] Kyle N. Baustert,[a] Jacob L. Hempel,[d] Alex M. Boehm,[a] Armin Ansary,[d] Douglas R. Strachan,[d] Jianguo Mei,[c] Chad Risko,[a,e] Vitaly Podzorov,[b] and Kenneth R. Graham*[a]

Author affiliations

*Corresponding author
[a]Department of Chemistry, University of Kentucky, Lexington, Kentucky 40506, USA **E-mail:** Kenneth.Graham@uky.edu
[b]Department of Physics and Astronomy, Rutgers University, Piscataway, New Jersey 08854, USA.
[c]Department of Chemistry, Purdue University, West Lafayette, Indiana 47907, USA
[d]Department of Physics & Astronomy, University of Kentucky, Lexington, Kentucky 40506, USA
[e]Center for Applied Energy Research, University of Kentucky, Lexington, Kentucky 40511, USA
[f]MH Catalyst, LLC, Lexington, Kentucky 40511, USA

This PDF file includes:

1. Experimental Data and Figures
Fig. S1 to S15
Table S1 to S5
2. Supplementary Discussion
S1 to S6

1. Experimental Data and Figures

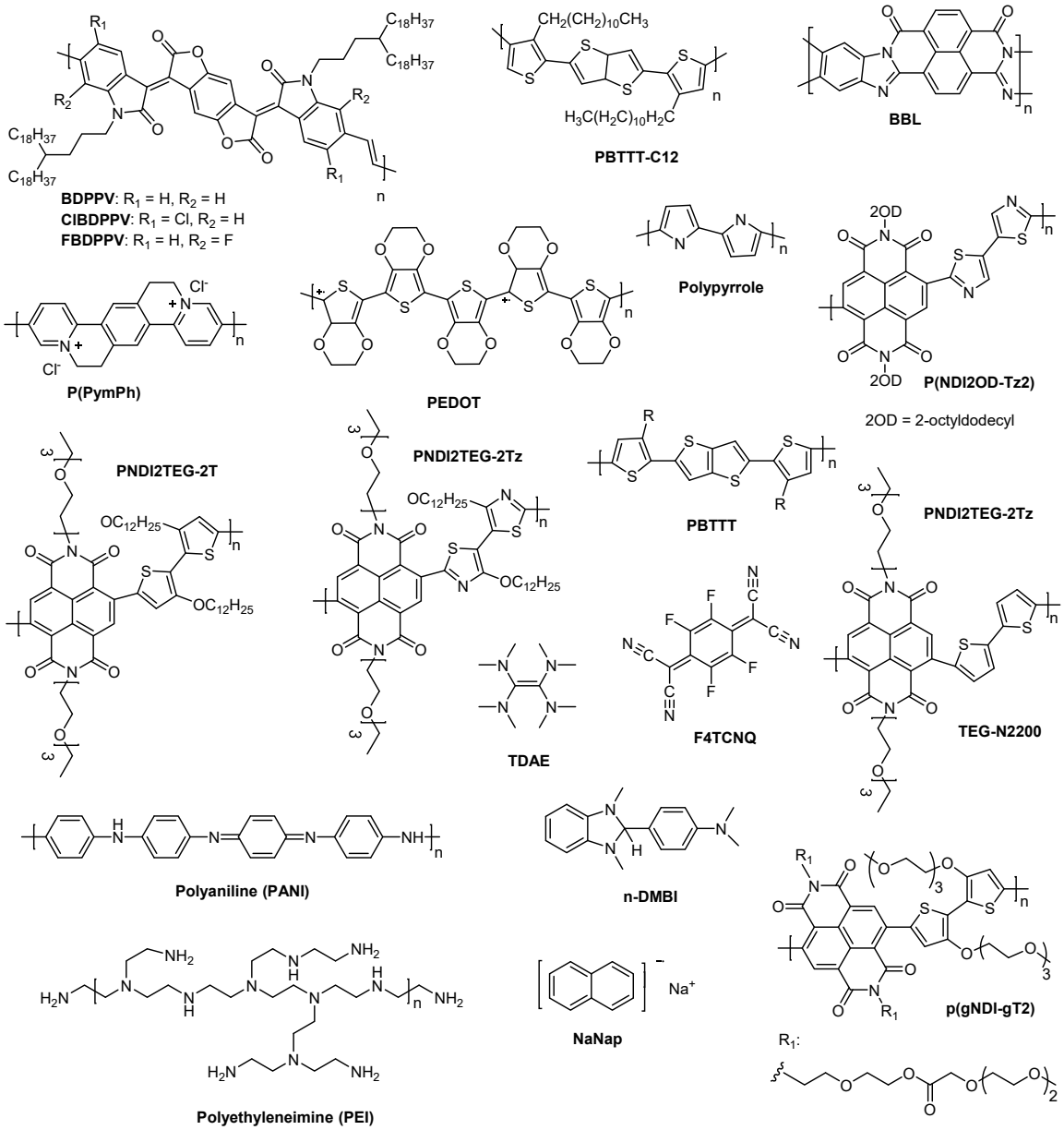

Fig. S1. Chemical structures of the various polymer and dopant acronyms listed in the manuscript and Supplementary Information.

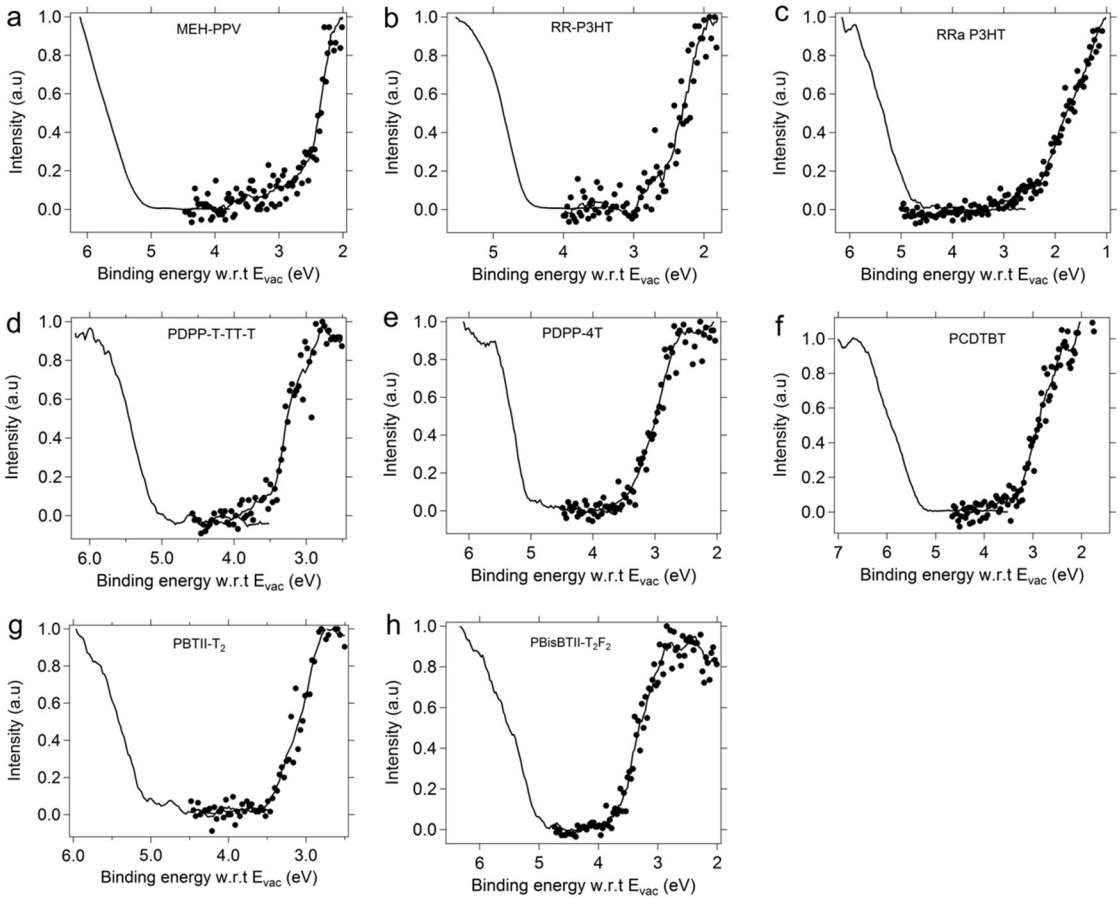

Fig. S2. UPS and IPES of pristine polymers. IPES data is shown with dots indicating each data point and solid lines showing a smoothed fit to the data using binomial smoothing. The UPS data (solid lines primarily at energies greater than E_F) is not smoothed. a) MEH-PPV; b) RR-P3HT; c) RRa-P3HT; d) PDPP-T-TT-T; e) PDPP-4T; f) PCDTBT; and g) PBTII-T_2, and h) PBisBTII-T_2F_2.

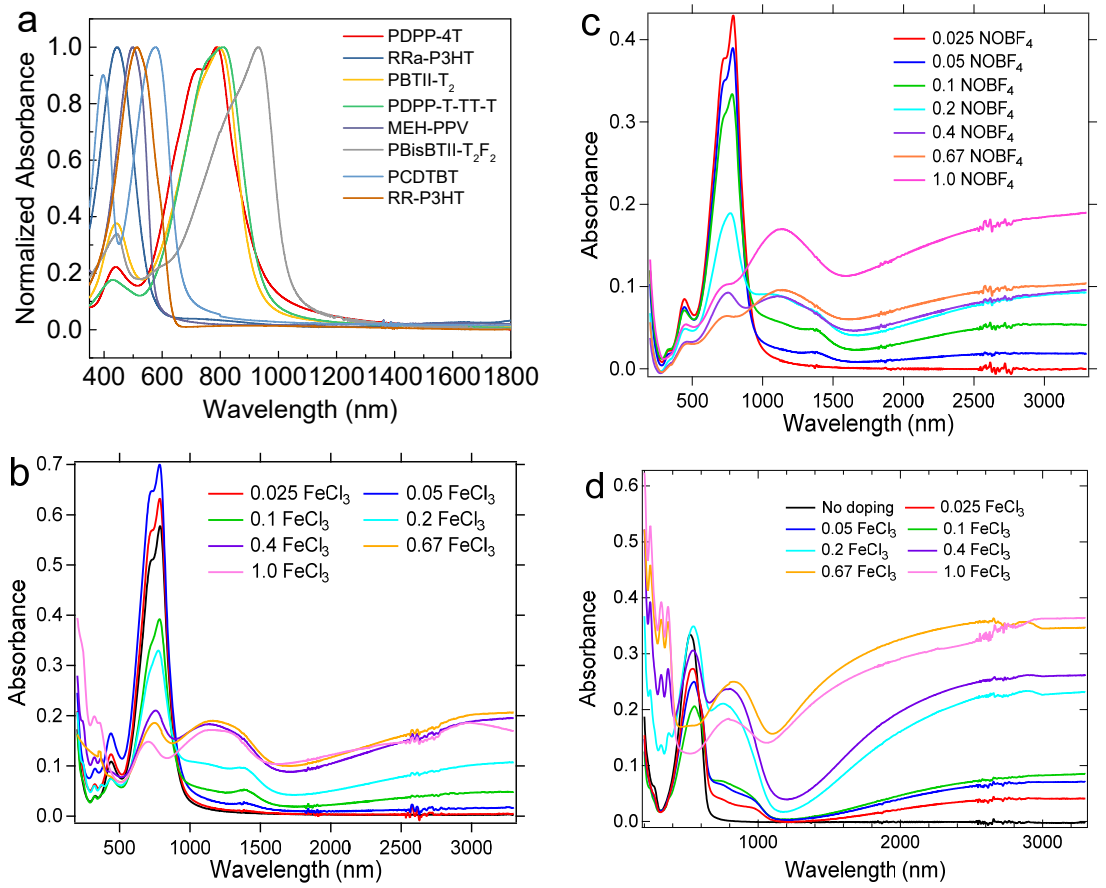

Fig. S3: UV-Vis-NIR absorbance spectra of all pristine polymers and PDPP-4T and RR-P3HT upon doping at varying concentrations. (**a**) UV-Vis-NIR absorbance spectra of all pristine polymer, (**b**) PDPP-4T upon doping with $FeCl_3$ and (**c**) upon doping with $NOBF_4$ at varying doping ratios. (**d**) $FeCl_3$ doped RR-P3HT at varying doping ratios. All films were prepared in a glovebox and measured outside of the glovebox in a linear transmission geometry. It is more relevant to compare the peak ratios as compared to the absolute absorbance, as the film thicknesses are all slightly different due to the effects of doping on solution viscosity and resulting film thickness. In (**a**) the effects of scattering were corrected for, but no correction for scattering was made in **b-d**.

Table S1. Experimentally measured IE, EA, band gap, and optical gap of all CPs included in this work.

Polymers	Electron affinity* (EA)(eV)	Ionization energy* (IE)(eV)	Work Function (E_f) (eV)	Transport gap (eV)	Optical gap (eV)
PDPP-4T	3.57	5.07	4.44	1.50	1.34
PDPP-T-TT-T	3.51	5.10	4.55	1.59	1.32
PBTII-T_2	3.49	5.12	4.60	1.63	1.35
PbisBTII-T_2F_2	3.68	5.03	4.55	1.35	1.20
PCDTBT	3.40	5.32	4.70	1.92	1.85
RR-P3HT	2.65	4.54	4.23	1.89	1.94
RRa-P3HT	2.59	4.84	4.59	2.25	2.23
MEH-PPV	2.80	5.22	4.77	2.42	2.15

*Uncertainty in the EA is ±0.08 eV and uncertainty in the IE is ±0.05 eV based on sample to sample variations and uncertainty associated with fitting the onset.

Table S2 Thermoelectric properties of doped *n*-type conjugated polymers

Polymer	D-A polymer	Dopant	Doping method	σ (S cm^{-1})	α (μV K^{-1})	PF_{max} (μW m^{-1} K^{-2})	change in sign of α
BBL[1]	no	TDAE	solution	1.2	-60	0.43	no
FBDPPV[2]	no	N-DMBI	solution	14	-140	28	no
PNDTI-BBT-DP[3]	no	N-DMBI	solution	5	-169	14	no
P(PymPh)[4]	no	NaNap	solution	18	-16.4	0.485	yes (n to p)
P(NDI2OD-Tz2)[1]	yes	TDAE	vapor	0.1	-447	1.5	no
TEG-N2200[5]	yes	N-DMBI	solution	0.17	-153	0.4	no
P(gNDI-gt2)[6]	yes	N-DMBI	solution	0.3	-93	0.4	no
P(NDIOD-T2)[7]	yes	N-DMBI	solution	0.008	-850	0.6	no
PDPF[8]	yes	N-DMBI	solution	1.3	-235	4.65	no
PNDI2TEG-2T[9]	yes	N-DMBI	solution	0.0007	57.2	0.0002	yes (n to p)
PNDI2TEG-2Tz[9]	yes	N-DMBI	solution	1.8	-159	4.6	no
PbisBTII-T_2F_2 (This work)	yes	$FeCl_3$	solution	0.28	-17	0.01	yes (p to n)
PBTII-T_2 (This work)	yes	$FeCl_3$	solution	11.5	-10.5	0.13	yes (p to n)
PDPP-T-TT-T (This work)	yes	$FeCl_3$	solution	0.042	-191.6	0.16	yes (p to n)
PCDTBT (This work)	yes	$FeCl_3$	solution	4.1	-24.5	0.25	yes (p to n)
PDPP-4T (This work)	yes	$FeCl_3$	solution	16.8	-74	9.2	yes (p to n)

Table S3: Adiabatic IE (AIE) and AEA of model oligomers as determined at the OT-ωPBE/6-31G(d,p) level of theory. Note that the optimally tuned ω value for each system is listed for reference.

Polymers	ω	AEA (eV)	AIE (eV)
PDPP-4T	0.126	2.17	5.57
PDPP-T-TT-T	0.123	2.25	5.61
PCDTBT	0.156	1.72	5.80
RR-P3HT	0.144	1.36	5.26
MEH-PPV	0.133	1.17	5.03

Table S4: Select frontier molecular orbital energies (eV) for the oligomers in the neutral state as determined at the OT-ωPBE/6-31G(d,p) level of theory.

	PDPP-T-TT-T	PDPP-4T	PCDTBT	RR-P3HT	MEH-PPV
LUMO	–2.15	–2.06	–1.53	–0.94	–1.01
HOMO	–5.69	–5.68	–6.11	–5.75	–5.22
HOMO–1	–5.89	–5.85	–6.26	–5.89	–5.37

In quantum chemistry, it is common to consider spin “restricted” and “unrestricted” molecular orbitals. In the spin restricted case, alpha and beta electrons are restrained to a single spatial orbital, and the terminology doubly occupied orbital is used. This scenario is generally used to describe the electronic structure of closed-shell (all electrons are paired) molecules. In the spin unrestricted case, the spatial-orbital restrictions on the spin alpha and spin beta electrons are lifted, and every electron occupies individual spatial orbitals. When the spin unrestricted scenario is used to describe a system with an even number of electrons, the resulting electronic structure is often quite like that described by the restricted calculations. Here, we are interested in describing what happens upon oxidation, where a chromophore (or segment of the polymer) in the thin film goes from an even number of electrons to an odd number of electrons. For the depiction of the electronic structure shown in Fig. 5, the black doubly occupied (and unoccupied) orbitals represent chromophores in the polymer matrix that have not been oxidized (closed shell); this scenario can be described by both spin restricted and unrestricted spatial orbitals, though we show only the former. Upon oxidation of a chromophore, we denote the singly occupied spin orbitals, which are energetically stabilized when compared to their initial energetic positions, in light blue, and the unoccupied spin orbitals (from which the electrons were removed), which are energetically destabilized, in dark blue; these situations are necessarily being described in the unrestricted sense.

Table S5: Select frontier molecular orbital energies (in eV) for the oligomers in the radical-cation state as determined at the OT-ωPBE/6-31G(d,p) level of theory. The molecular orbitals, apart from the lowest unoccupied spin orbital (LUSO) from which the electron was removed upon oxidation, are reported in a parlance consistent with the naming used for the neutral state. The alpha (α) and beta (β) spins are explicitly denoted.

	PDPP-T-TT-T		PDPP-4T		PCDTBT		RR-P3HT		MEH-PPV	
	α	β	α	β	α	β	α	β	α	β
LUMO	–4.25	–4.13	–4.33	–4.15	–4.19	–4.00	–3.20	–3.09	–3.42	–3.32
LUSO		–5.39		–5.36		–5.64		–4.80		–5.07
HOMO	–6.90	–6.87	–6.67	–6.66	–7.24	–7.20	–6.37	–6.33	–6.90	–6.82
HOMO–1	–7.36	–7.15	–7.03	–6.96	–7.45	–7.44	–6.53	–6.50	–7.13	–7.09

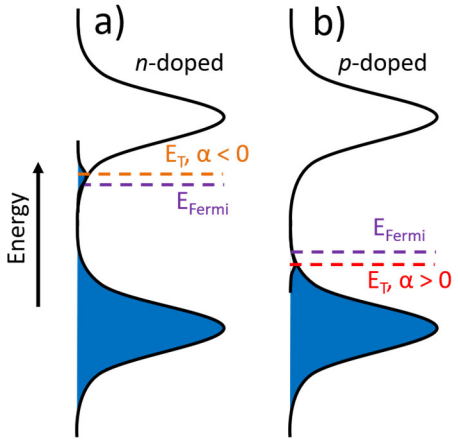

Fig. S4. Schematic DOS distributions with Fermi energies and transport energies indicated. (**a**) DOS for an *n*-doped semiconductor and (**b**) a *p*-doped semiconductor.

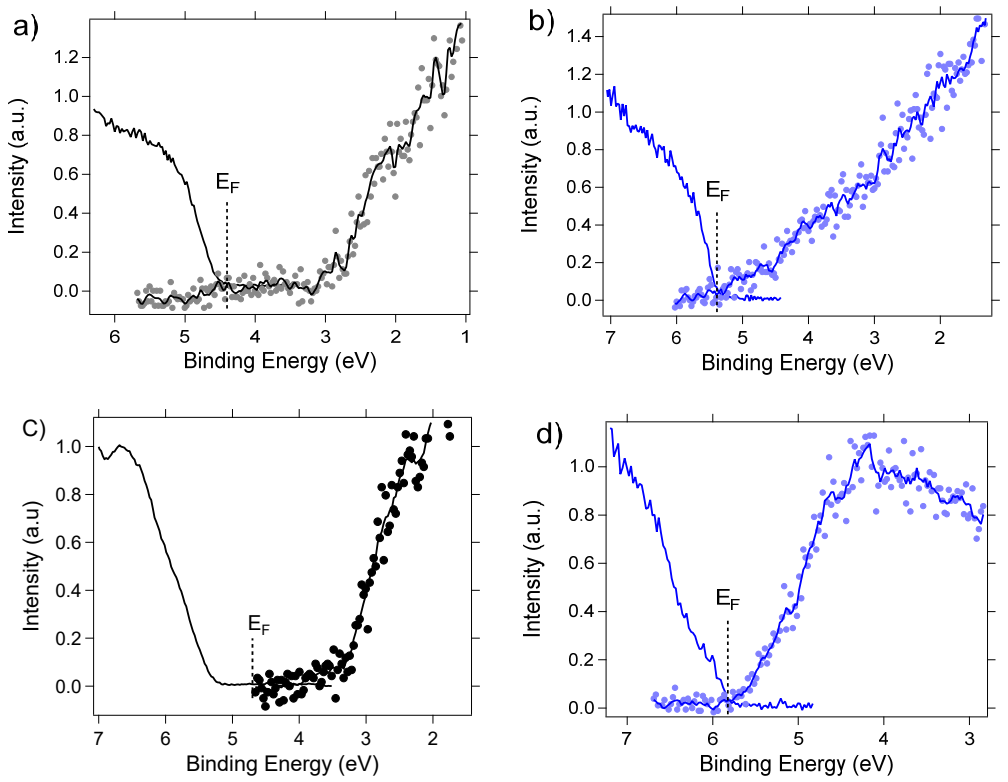

Fig. S5. UPS and IPES spectra of RR-P3HT and PCDTBT with no doping and with $FeCl_3$ doping. IPES data is shown with dots indicating each data point and solid lines indicating a smoothed fit to the data using binomial smoothing. The UPS data (solid lines primarily at energies greater than E_F) is not smoothed. Plots (**a**) and (**b**) are of RR-P3HT with 0 (**a**) and 0.43 (**b**) $FeCl_3$ doping ratios and plots (**c**) and (**d**) are of PCDTBT with 0 (**c**) and 1.29 (**d**) $FeCl_3$ doping ratios. Both (**b**) and (**d**) show that the occupied and unoccupied states converge for RR-P3HT and PCDTBT at relatively high $FeCl_3$ doping ratios.

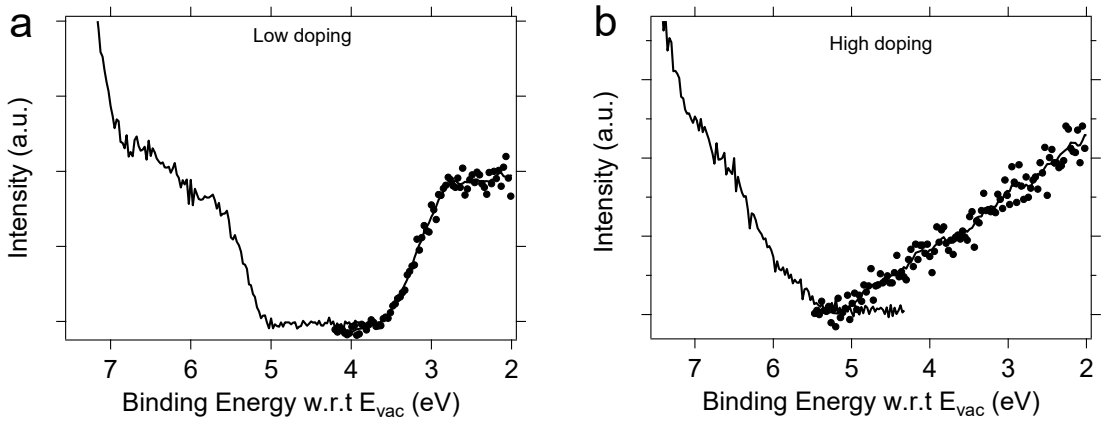

Fig. S6. UPS and IPES spectra of $NOBF_4$ doped PDPP-4T. (**a**) With a 0.02 doping ratio and (**b**) 0.67 doping ratio. IPES data is shown with dots indicating each data point and solid lines indicating a smoothed fit to the data using binomial smoothing. The UPS data (solid lines primarily at energies greater than E_F) is not smoothed.

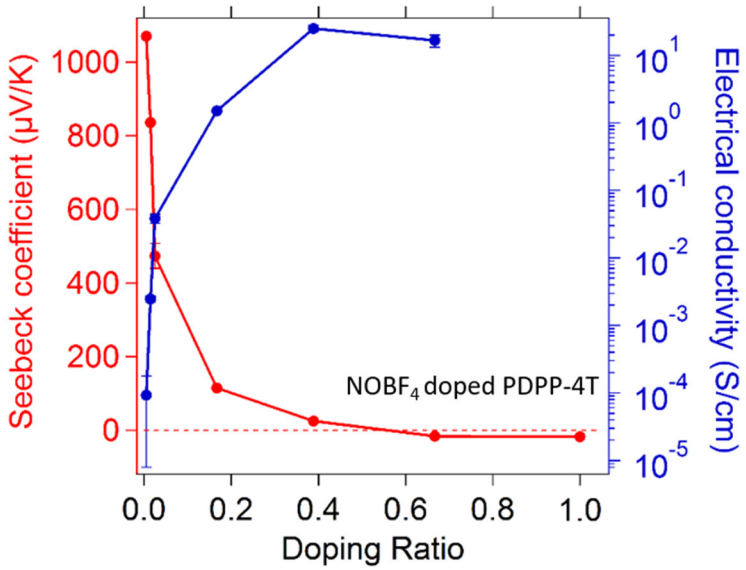

Fig. S7. Seebeck coefficient and electrical conductivity for $NOBF_4$ doped PDPP-4T. Error bars are equal to ± one standard deviation from three to six individual samples measured for each doping ratio.

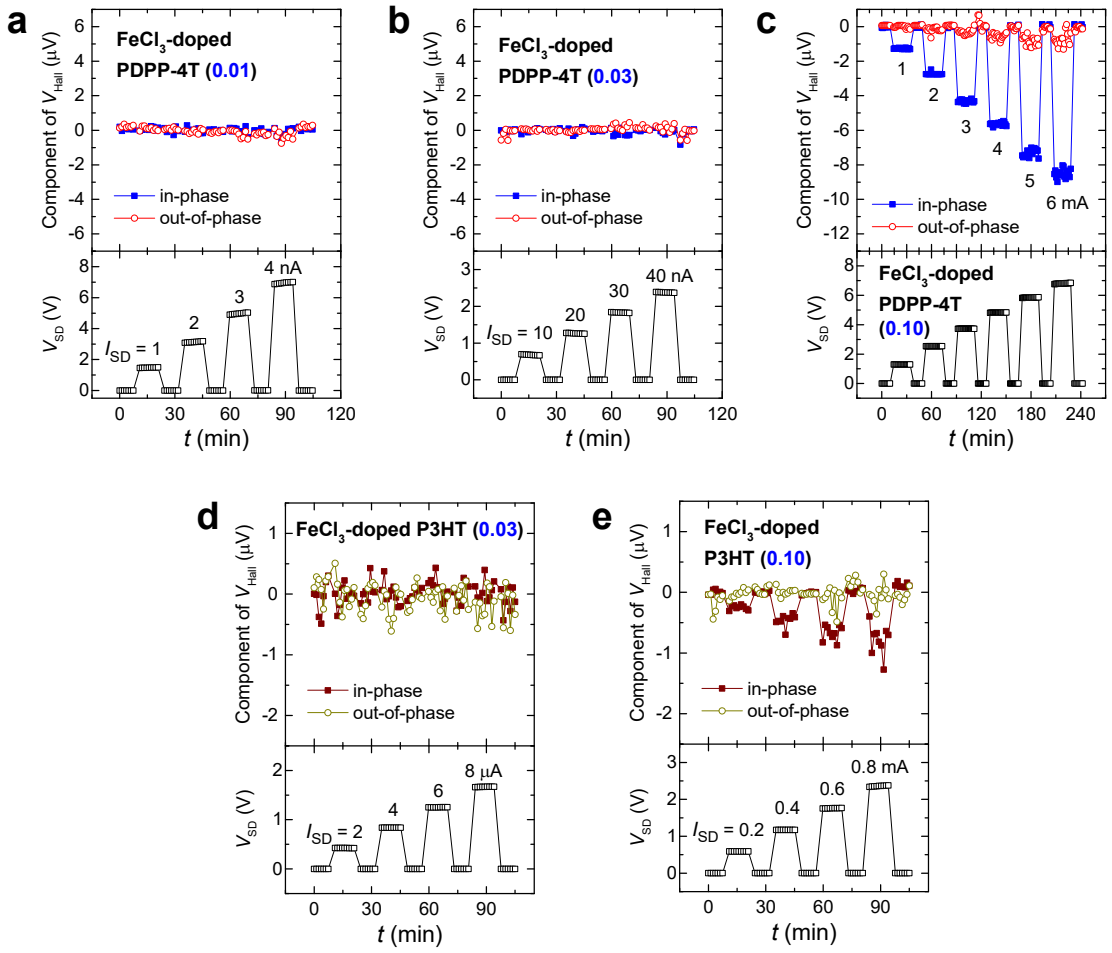

Fig. S8. *ac*-Hall effect measurements of PDPP-4T (panels **a**, **b** and **c**) and P3HT (panels **d** and **e**) polymer films doped with $FeCl_3$ from low to medium doping ratios. The in-phase (solid symbols) and out-of-phase (open symbols) components of the *ac*-Hall voltage, V_{Hall}, are shown in the upper panels. The applied source-drain *dc*-voltage, V_{SD}, and the corresponding source-drain excitation current, I_{SD}, are shown in the lower panels. The doping ratio, defined as the ratio of the molar concentrations of $FeCl_3$ dopant and aromatic rings of the polymer, are indicated in parentheses in blue. The on&off cycling of I_{SD} is performed intentionally to determine the zero-current background of the Hall voltage (note: this cycling has nothing to do with the *ac* measurement technique used here, and it can be aperiodic). These results show that no Hall effect is observed at low doping ratios (< 0.1), while at the doping ratio ≈ 0.1, a Hall effect starts emerging, and the sign of the Hall voltage is negative, signifying that electrons are the dominant mobile (delocalized) charge carriers.

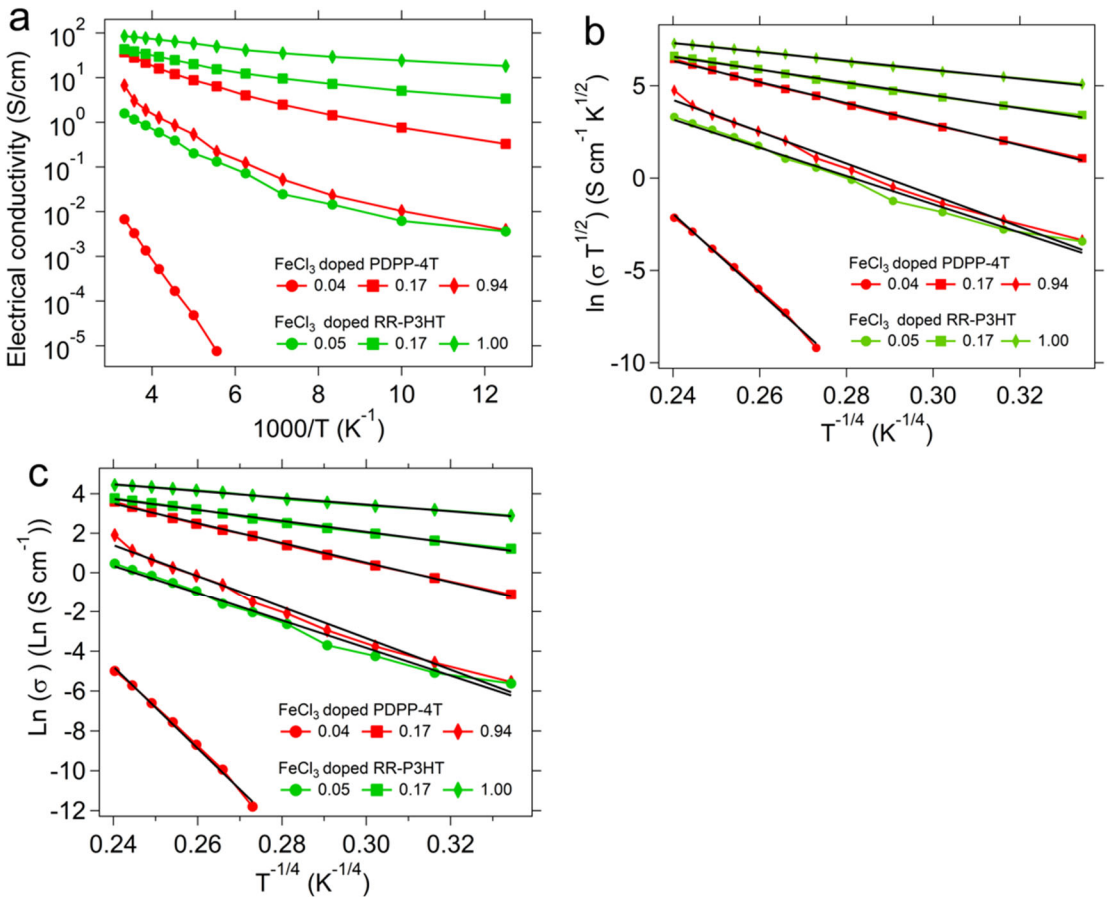

Fig. S9: Temperature dependent electrical conductivity of $FeCl_3$ doped RR-P3HT and PDPP-4T polymers presented in different manners to highlight fits to various transport models. (**a**) σ vs 1000 T^{-1}, (**b**) with variable hopping mechanism, ln $\sigma T^{1/2}$ vs. $T^{-1/4}$ and (**c**) with Mott variable hopping mechanism, (d=3) ln σ vs. $T^{-1/4}$. For all fits, the linear fitting coefficient R^2 is greater than 0.98. The data fits suggest that in all cases hopping-type transport is the limiting mechanism.

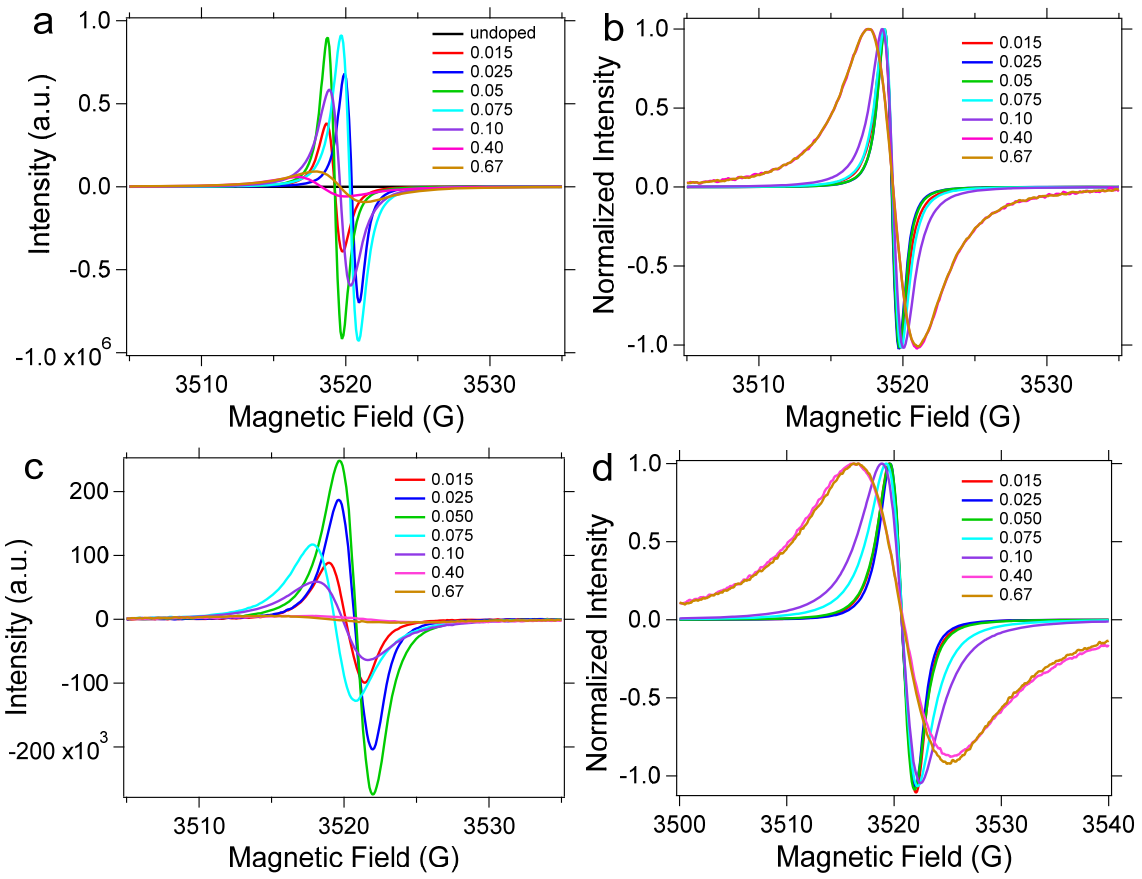

Fig. S10. Electron paramagnetic resonance (EPR) spectra of $NOBF_4$ doped PDPP-4T (**a** and **b**), and $NOBF_4$ doped RR-P3HT (**c** and **d**). Spectra in (**a**) and (**c**) are not normalized, whereas in spectra (**b**) and (**d**) the spectra have been normalized in intensity and shifted in x such that the zero crossing points line up to allow for more direct comparison between peak widths. The peak areas do not correspond directly with the number of unpaired electrons, as Q must be accounted for. Q values range from 10,800 for undoped PDPP-4T to 5300 for PDPP-4T with a 0.67 doping ratio and from 11,000 for RR-P3HT with a doping ratio of 0.015 to 3,300 for RR-P3HT with a doping ratio of 0.67.

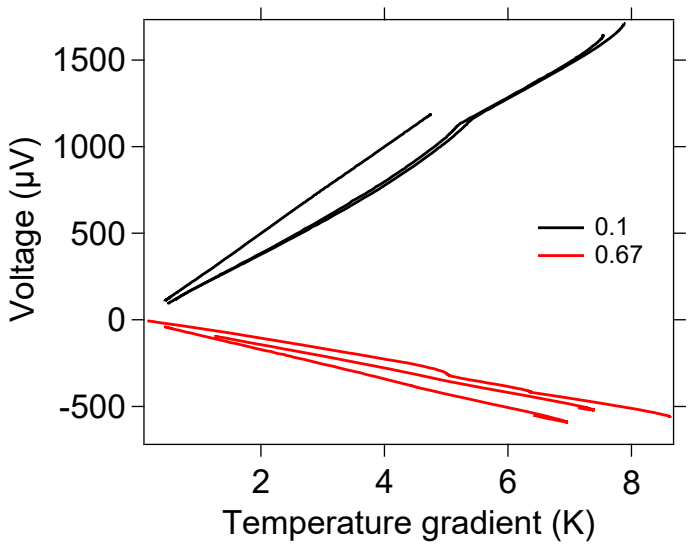

Fig. S11. Voltage vs. temperature data for $FeCl_3$ doped PDPP-4T with 0.10 and 0.67 doping ratios. The different traces correspond to different films.

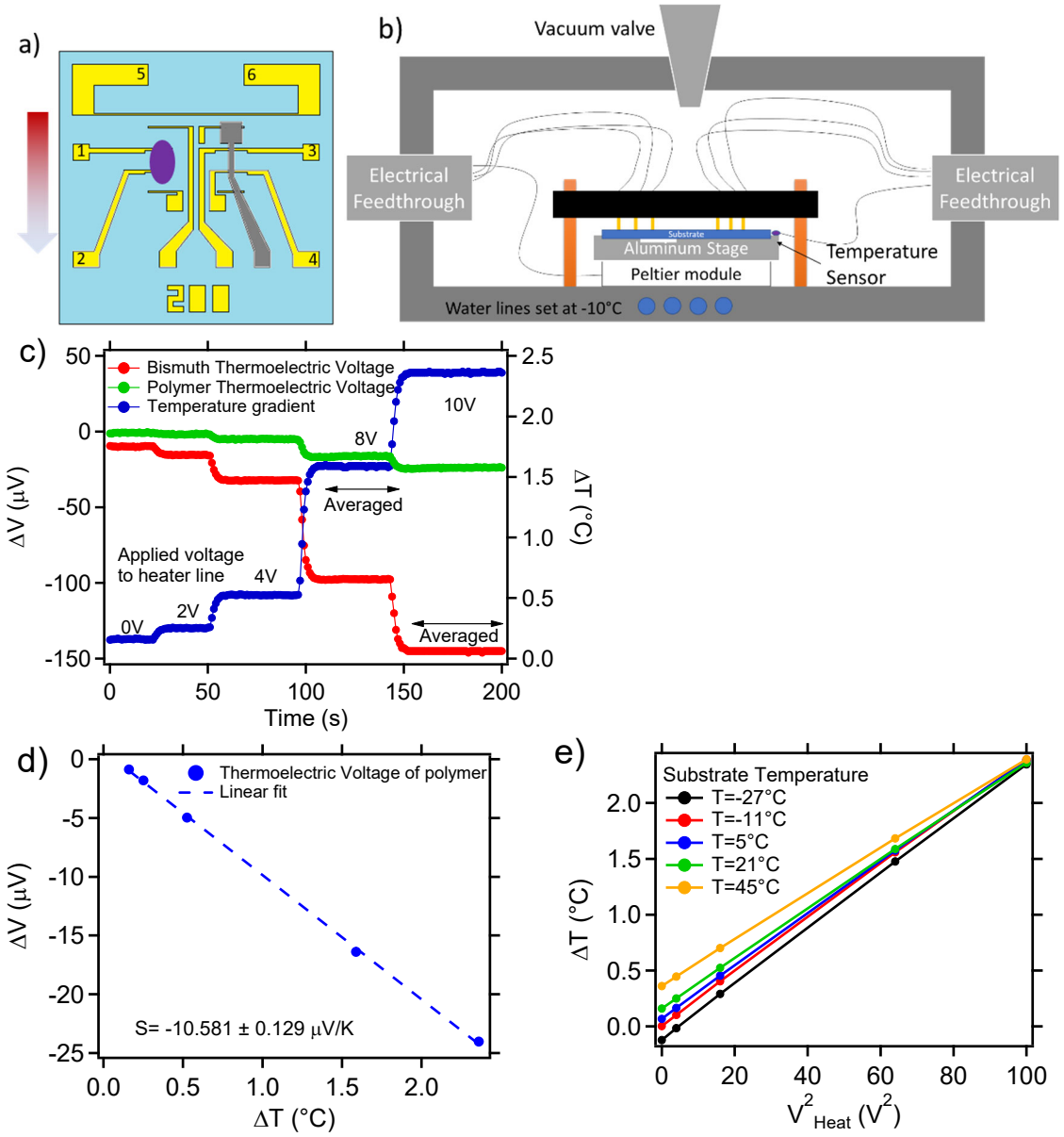

Fig. S12. Schematics and data for the temperature dependent Seebeck coefficient measurements. (**a**) Schematic of the device structure and (**b**) vacuum chamber for temperature dependent Seebeck measurements. (**c**) Thermoelectric voltage of bismuth (red) and representative CP film (green) as a function of time with varying applied heater line power (each step corresponds to a different power input and the applied voltage is shown next to each step). The temperature gradient is calculated based on the voltage of the bismuth film. (**d**) Average thermoelectric voltage of polymer film versus average temperature at each power increment applied to the heater line. (**e**) Temperature gradient versus applied voltage to heater line squared (proportional to power) at different substrate temperatures.

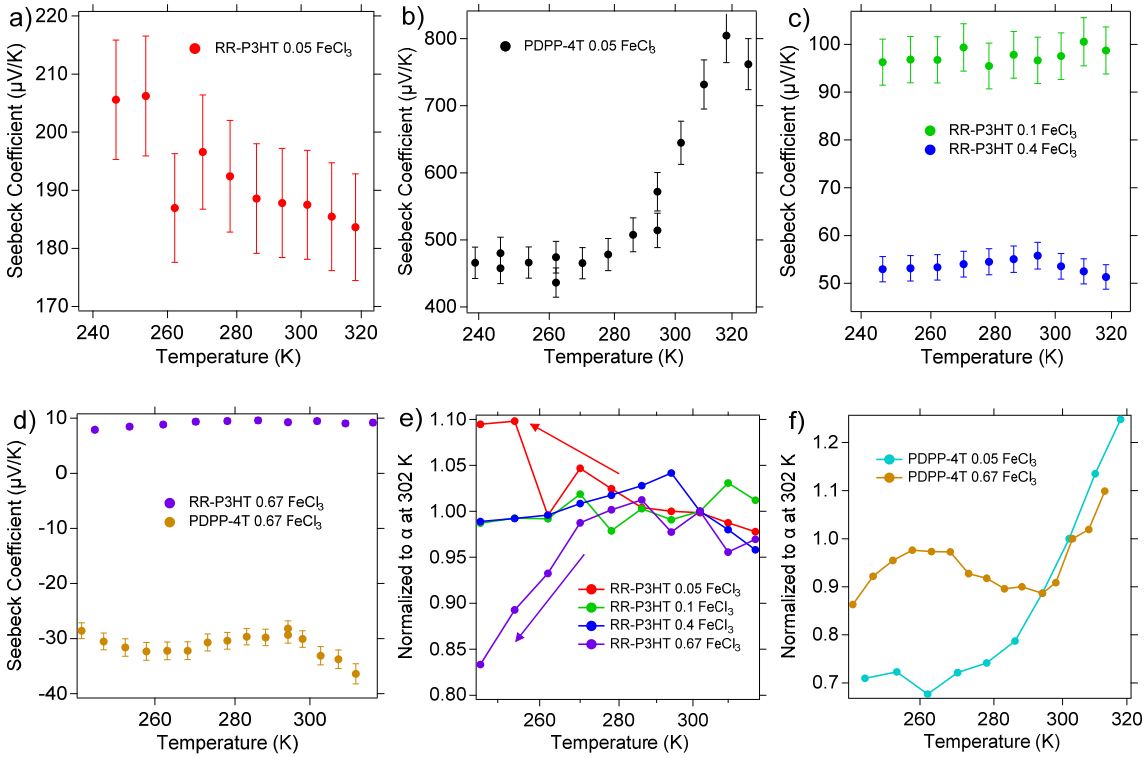

Fig. S13. Temperature dependent Seebeck coefficient measurements for RR-P3HT and PDPP-4T at varying $FeCl_3$ doping ratios. RR-P3HT at 0.05 (**a**), PDPP-4T at 0.05 (**b**), RR-P3HT at 0.1 and 0.4 (**c**), and RR-P3HT and PDPP-4T at 0.67 (**d**) doping ratios. Panels (**e**) and (**f**) show the normalized Seebeck coefficient (normalized to α at 302 K) for the RR-P3HT samples (**e**) and the PDPP-4T samples (**f**). Error bars are equal to ± 5% of the measured value. The data in (**e**) and (**f**) does not include error bars to enable easier readability. Error bars are found for those data points in (**a-d**).

2. Supplemental Discussion

S1:

Equation 1 used in the manuscript can be further expanded to provide more insight into how the Seebeck coefficient is determined. Equation S1 presents an expanded version where $\sigma_S(E,T)$ is the electrical conductivity spectrum and f_{FD} is the Fermi Dirac function.[10]

$$\alpha(T) = -\frac{k}{q}\frac{\int(\frac{E-E_F}{kT})\sigma_S(E,T)\left[-\frac{\partial f_{FD}(E,T)}{\partial E}\right]dE}{\int \sigma_S(E,T)\left[-\frac{\partial f_{FD}(E,T)}{\partial E}\right]dE} \quad \text{Equation S1}$$

Here, $\sigma_S(E,T)$ is a function of the density of states, *g(E,T),* and the mobility, *μ(E,T)*. Equation S1 is related to equation 1 in the manuscript in that $\sigma(E,T) = \sigma_S(E,T)\left[-\frac{\partial f_{FD}(E,T)}{\partial E}\right] = qg(E,T)\mu(E,T)\left[-\frac{\partial f_{FD}(E,T)}{\partial E}\right]$, with *q* being the elementary charge. In the situation where both occupied and unoccupied states converge near E_F, the sign of *α* will depend on *g(E,T)* and *μ(E,T)* near E_F. In the case proposed for most of the CPs in this work (i.e., the semi-crystalline polymers) charge carriers in the crystalline regions will display much higher *μ(E)* than the amorphous regions; however, this is only one aspect determining *α*. The energy relative to E_F for both the amorphous and crystalline regions' contributions to the DOS will also act to determine the sign of *α* in these systems.

To illustrate how the relative positions of the various contributions to the DOS can impact the sign of *α*, Fig. S14a and c present example DOS plots, the numerator of Equation S1, and the sign of *α*. The colors in the DOS plots correspond to Fig. 5b in the manuscript, where the solid black Gaussian represents singly and doubly occupied states, the dashed black Gaussian represents unoccupied states, and the orange Gaussian represents the bipolaron and lowest unoccupied spin orbital (LUSO) band. In Fig. S14a the occupied state distribution is 0.2 eV closer to E_F than in Fig. S14c and all other parameters are equal. Qualitatively, Fig. S14a represents what the UPS results show for heavily doped RR-P3HT while Fig. S14c represents PDPP-4T. Overlaid UPS and IPES spectra for heavily doped RR-P3HT and PDPP-4T are presented in Fig. S15. We present this UPS and IPES data along with potential DOS distributions to highlight potential factors that can influence the sign of *α*, we do not intend for this to be a definitive explanation as to why RR-P3HT does not show a negative *α* and PDPP-4T does. In Fig. S14a the occupied state distribution lies closer to E_F and a positive *α* is calculated, whereas in Fig. S14c the occupied state distribution is 0.2 eV further from E_F and a negative *α* is calculated. These scenarios treat $\sigma_S(E,T) = g(E,T)$ and neglect charge-carrier mobility differences; however, as discussed previously, the charge-carrier mobilities are likely to vary significantly between the amorphous and crystalline regions and these differences are expected to have a drastic influence on the Seebeck coefficient.

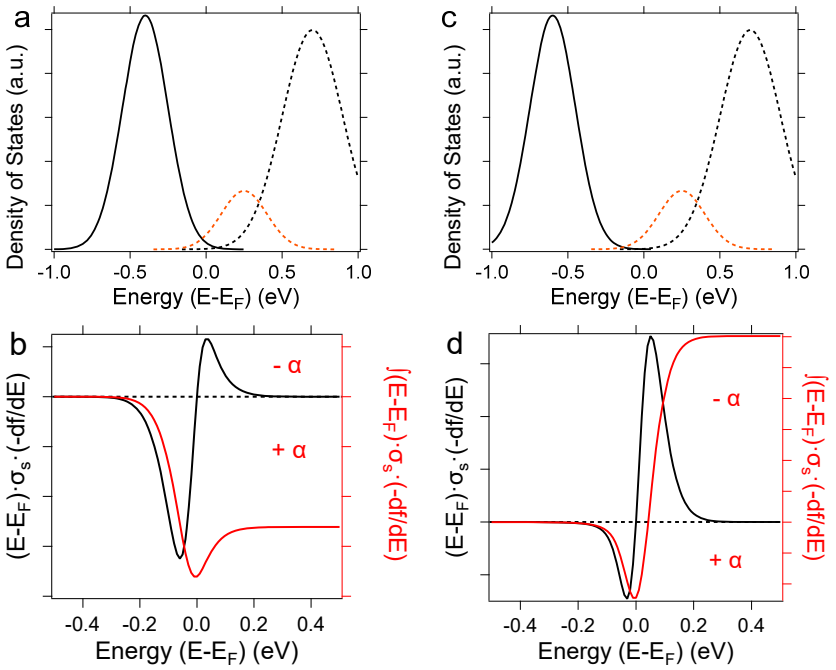

Fig. S14. DOS schematics (**a** and **c**) for two different polymers and calculated parameters (**b** and **d**) from Equation S1 that show how the sign of the Seebeck coefficient can differ between the two polymers. The difference in the DOS distributions of the two polymers is only that the occupied state distribution is shifted by 0.2 eV between (**a**) and (**c**). The colors in the DOS plots correspond to Fig. 5b in the manuscript, where the solid black Gaussian represents singly and doubly occupied states, the dashed black Gaussian represents unoccupied states, and the orange Gaussian represents the bipolaron and LUSO band. Plots (**b**) and (**d**) show the numerator of Equation S1, the integrand is shown in black and the integral is shown in red. In plots (**b**) and (**d**) the dashed black line is the zero line for both the left and right axes.

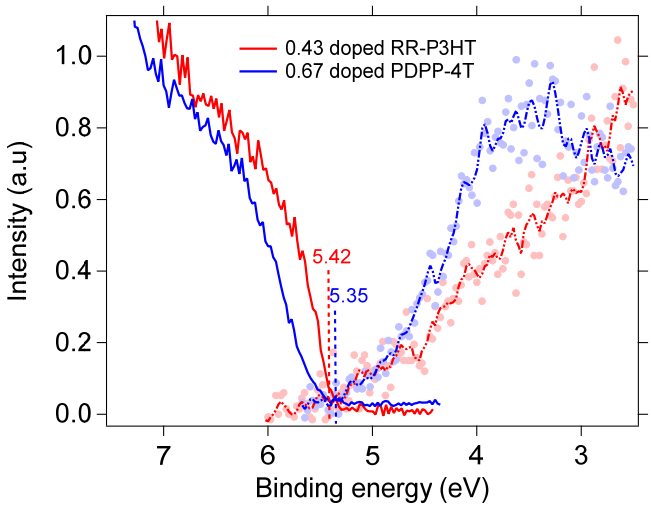

Fig. S15. Overlaid UPS and IPES spectra highlighting the differences between RR-P3HT (red) and PDPP-4T (blue) at 0.43 and 0.67 doping concentrations, respectively. The dashed red and blue lines at 5.42 and 5.35 eV indicate the position of E_F vs. vacuum for RR-P3HT and PDPP-4T, respectively. Solid lines indicate UPS data, dots indicate individual IPES data points, and the dotted and dashed lines show a smoothed fit to the IPES data using binomial smoothing.

S2:

To probe whether states on $FeCl_3$ may be responsible for the IPES signal extending to E_F, we doped PDPP-4T with $NOBF_4$. $NOBF_4$ also results in *p*-doped PDPP-4T, and PDPP-4T doped with $NOBF_4$ at a 0.67 doping ratio shows similar UPS and IPES spectra as the $FeCl_3$ doped sample, as shown in Supplementary Fig. S6. As NO (nitric oxide) is expected to evaporate from the sample after oxidizing the polymer,[11] the signal near E_F is not likely from NO. The similar convergence of the occupied and unoccupied distributions of states near E_F indicates that the UPS and IPES signals near E_F are primarily from the polymer. Importantly, $NOBF_4$ doping shows similar trends as $FeCl_3$ doping in the UV-Vis-NIR absorbance spectra, σ, and α as the $FeCl_3$ doped samples (Supplementary Fig. S3c and S7).

In regards to the UPS and IPES data, the polarization energies in the films are significant (typically around 1 eV) and the measured IE and EA can also be influenced by molecular orientation and surface dipoles.[12] By contrast, the energy states of charge carriers within the film and polarization energies associated with these charge carriers would not be as influenced by molecular orientations and surface dipoles. Although differences in orientation and surface dipoles can result in an apparent shift in the IE and EA, and thus the polarization energy would appear to change as well, these effects should impact both the IE and EA equally.[12] Thereby, the transport gap measured with photoelectron spectroscopy should be comparable to the energy difference between electrons and holes at the band edges within the film.

S3:

In the context of this manuscript we use band-like transport to refer to charge carriers that are significantly delocalized such that they form extended or quasi-extended states. This contrasts with another definition of band-like transport based on a more traditional interpretation, where the characteristic signature of band-like transport is an increase in the charge-carrier mobility with decreasing temperature. Sufficiently delocalized carriers, which we refer to as band-like, will experience the Lorentz force, even if only temporarily, since they should gain microscopic velocity while being delocalized, and thus contribute to the Hall voltage. Therefore, the primary important factor for the observation of a Hall effect in organic semiconductors is not having a negative slope of mobility(T) dependence, but rather to have carrier delocalization over some appreciable length scale.

S4:

In addition to revealing the carrier type, the Hall effect measurements provide an estimate for the charge-carrier mobilities (μ_{Hall} = 0.05 – 0.3 $cm^2V^{-1}s^{-1}$) and the carrier densities (n_{Hall} = (3.5 – 8)$\times10^{20}$ cm^{-3}) in doped polymers investigated in this study (Fig. 4 in paper). One should keep in mind though that these values do not necessarily represent the mobility of individual mobile (that is, delocalized) carriers or their actual density. A Hall voltage in heavily disordered systems forms as a result of a competition between subpopulations of band-like and hopping carriers, coexisting in a sample.[13] Therefore, these values can only be used for relative sample comparison. It is also worth noting that Hall effect measurements carried out for the polymer PBTTT, doped with a different strong electron acceptor (F4TCNQ), using the same *ac*-Hall apparatus revealed *p*-type charge transport.[14] This lends credibility to the observation of an electron-type Hall effect in this work, but shows that the emergence of electron conduction in an electron acceptor-doped

polymer, although occurring in many systems, still depends on the type of the host matrix, the dopant and the doping level.

S5:

A series of experiments were carried out to explore if $FeCl_3$ was responsible for the observed electron conduction in the $FeCl_3$-doped polymer films. The first point of evidence against $FeCl_3$ phases leading to electron transport arises from the assumption that if $FeCl_3$ contributes to transport, then the change from positive to negative Seebeck coefficients should occur for any CP that can be heavily doped with $FeCl_3$. However, we see that for RR-P3HT, RRa-P3HT, and MEH-PPV the Seebeck remains positive with $FeCl_3$ doping at all concentrations. The electrical conductivity due to $FeCl_3/FeCl_3^-$ should be relatively similar in all polymers, with some variation expected due to morphology and doping efficiency. In this case, polymers with lower electrical conductivities should be more likely to show negative Seebeck coefficients with high $FeCl_3$ loading, as the $FeCl_3$ component would be contributing more to the total electrical conductivity. However, some polymers with lower electrical conductivities, such as RRa-P3HT and MEH-PPV, do not show negative Seebeck coefficients. Another point of evidence is that if electron transport through $FeCl_3$ was dominating the electrical conductivity, then we should see that pure $FeCl_3$, $FeCl_2/FeCl_3$ blends, or partially reduced $FeCl_3^-/FeCl_3$ films show electrical conductivities that approach those for the $FeCl_3$ doped polymers. However, we see that in all cases the electrical conductivity remains two to five orders of magnitude lower than what is observed for the $FeCl_3$ doped conjugated polymers. The electrical conductivity of pure $FeCl_3$ and $FeCl_3/FeCl_2$ blends is $<1\times10^{-3}$ S cm^{-1} for pure $FeCl_3$ and $FeCl_3/FeCl_2$ blends vs. 0.1 to 56 S/cm for highly doped polymers. These $FeCl_3/FeCl_2$ films were fabricated with and without the presence of an insulating polymer host (polyethyleneimide) to further manipulate the $FeCl_3/FeCl_2$ morphology and connectivity, but electrical conductivities remained $<1\times10^{-3}$ S/cm. Partially reduced $FeCl_3$ films were fabricated using Spiro-OMeTAD as the reducing agent. Here, Spiro-OMeTAD is a low mobility (~1×10^{-4} cm^{2}V^{-1}s^{-1}) small organic molecule with an IE of 5.06 eV[15] that will lead to the introduction of $FeCl_3^-$ states without allowing significant hole transport through the Spiro-OMeTAD. These blends showed electrical conductivities of <0.05 S/cm, which further supports that it is unlikely that $FeCl_3/FeCl_3^-$ can contribute to the electrical conductivity enough to influence the Seebeck coefficient in the doped polymers.

To further rule out the possibility that the negative Seebeck coefficients arise due to transport through $FeCl_3$, we looked at $NOBF_4$ doping. $NOBF_4$ doping of PDPP-4T at 0.67 and 1.0 doping ratios also results in negative α (Supplementary Fig. S7). The fact that both $FeCl_3$ and $NOBF_4$ dopants lead to negative Seebeck coefficients, combined with the previously discussed points regarding transport through $FeCl_3$, strongly support that charge transport is dominated by the conjugated polymers. Furthermore, the fact that multiple dopants can lead to *n*-type behavior in *p*-doped CPs shows the generality of this approach.

S6:

The temperature dependence of α can provide more insight into the transport mechanism in materials. It has been reported that semi-crystalline polymers can show a combination of transport behavior and the temperature dependent α measurements can be fit based on Equation S2.[16-18]

$$\alpha = A_1 + \frac{A_2}{T} + A_3\sqrt{T} + A_4T \qquad \text{Equation S2}$$

Here A_1, A_2, A_3 and A_4 are fitting parameters and T is temperature in K. Metallic type transport shows a linear response of the Seebeck coefficient to temperature, 3D variable range hopping transport shows a square root response to temperature, and 1D hopping type transport shows an inverse dependence of α on temperature. Our temperature dependent measurements cover a range of 70K (246 to 318 K) for two different polymers, RR-P3HT and PDPP-4T, doped with $FeCl_3$. Given the limited range of our temperature dependent α measurements, we evaluate the data more qualitatively. Fig. S13e shows temperature dependent Seebeck coefficient measurements for RR-P3HT doped with $FeCl_3$ normalized to their value at 302 K. As temperature decreases, α for 0.05% doped P3HT increases which suggests that 1D hopping transport is dominant. At concentrations of 0.1 and 0.4 α is nearly flat with temperature, which is not entirely consistent with pure metallic or pure hopping type transport. At these intermediate doping concentrations both transport mechanisms could be playing a significant role, potentially counteracting each other to lead to a near temperature independent α over the temperature range probed. At the highest doping ratio of 0.67, the behavior becomes slightly more metallic in nature as α decreases slightly with decreasing temperature. However, the temperature dependence of α is still not fully metallic, as the decrease in α is only observed below 270 K. For PDPP-4T the 0.05 doped sample shows a large increase in α beyond 280 K, but below 280 K α shows smaller variation. Such behavior is again inconsistent with one form of transport. The PDPP-4T 0.67 $FeCl_3$ doped sample does not show a clear trend in α with varying temperature, as α shows slow oscillations over the temperature range probed. In general, these temperature dependent Seebeck measurements are supportive of mixed transport mechanisms, but they also highlight the need for measurements to be conducted over a broader temperature range to obtain further insight.

References:

1. Wang, S., Sun, H., Erdmann, T., Wang, G., Fazzi, D., Lappan, U.*, et al.* A Chemically Doped Naphthalenediimide-Bithiazole Polymer for n-Type Organic Thermoelectrics. *Adv. Mater.*, **30,** 1801898 (2018).
2. Shi, K., Zhang, F., Di, C.-A., Yan, T.-W., Zou, Y., Zhou, X.*, et al.* Toward High Performance n-Type Thermoelectric Materials by Rational Modification of BDPPV Backbones. *J. Am. Chem. Soc.*, **137,** 6979-6982 (2015).
3. Wang, Y., Nakano, M., Michinobu, T., Kiyota, Y., Mori, T., Takimiya, K. Naphthodithiophenediimide–Benzobisthiadiazole-Based Polymers: Versatile n-Type Materials for Field-Effect Transistors and Thermoelectric Devices. *Macromolecules*, **50,** 857-864 (2017).
4. Hwang, S., Potscavage, W. J., Yang, Y. S., Park, I. S., Matsushima, T., Adachi, C. Solution-processed organic thermoelectric materials exhibiting doping-concentration-dependent polarity. *PCCP*, **18,** 29199-29207 (2016).
5. Liu, J., Qiu, L., Alessandri, R., Qiu, X., Portale, G., Dong, J.*, et al.* Enhancing Molecular n-Type Doping of Donor–Acceptor Copolymers by Tailoring Side Chains. *Adv. Mater.*, **30,** 1704630 (2018).
6. Kiefer, D., Giovannitti, A., Sun, H., Biskup, T., Hofmann, A., Koopmans, M.*, et al.* Enhanced n-Doping Efficiency of a Naphthalenediimide-Based Copolymer through Polar Side Chains for Organic Thermoelectrics. *ACS Energy Lett.*, **3,** 278-285 (2018).
7. Schlitz, R. A., Brunetti, F. G., Glaudell, A. M., Miller, P. L., Brady, M. A., Takacs, C. J.*, et al.* Solubility-Limited Extrinsic n-Type Doping of a High Electron Mobility Polymer for Thermoelectric Applications. *Adv. Mater.*, **26,** 2825-2830 (2014).

8. Yang, C.-Y., Jin, W.-L., Wang, J., Ding, Y.-F., Nong, S., Shi, K.*, et al.* Enhancing the n-Type Conductivity and Thermoelectric Performance of Donor–Acceptor Copolymers through Donor Engineering. *Adv. Mater.*, **30,** 1802850 (2018).
9. Liu, J., Ye, G., Zee, B. v. d., Dong, J., Qiu, X., Liu, Y.*, et al.* N-Type Organic Thermoelectrics of Donor–Acceptor Copolymers: Improved Power Factor by Molecular Tailoring of the Density of States. *Adv. Mater.*, **30,** 1804290 (2018).
10. Rowe, D. M. Thermoelectric and its energy harvesting: Materials, Preparation, and Characterization in Thermoelectrics, 1st Edition. *CRC press* (2016).
11. Guerrero, A., Boix ,P. P., Marchesi, L. F., Ripolles-Sanchis, T., Pereira, E. C., Garcia-Belmonte, G. Oxygen doping-induced photogeneration loss in P3HT:PCBM solar cells. *Sol. Energy Mater. Sol. Cells*, **100,** 185-191 (2012).
12. Yoshida, H., Yamada, K., Tsutsumi, J. y., Sato, N. Complete description of ionization energy and electron affinity in organic solids: Determining contributions from electronic polarization, energy band dispersion, and molecular orientation. *Phys. Rev. B*, **92,** 075145 (2015).
13. Yi, H. T., Gartstein, Y. N., Podzorov, V. Charge carrier coherence and Hall effect in organic semiconductors. *Sci. rep.*, **6,** 23650 (2016).
14. Fujimoto, R., Watanabe, S., Yamashita, Y., Tsurumi, J., Matsui, H., Kushida, T.*, et al.* Control of molecular doping in conjugated polymers by thermal annealing. *Org. Electron.*, **47,** 139-146 (2017).
15. Park, S. M., Mazza, S. M., Liang, Z., Abtahi, A., Boehm, A. M., Parkin, S. R.*, et al.* Processing Dependent Influence of the Hole Transport Layer Ionization Energy on Methylammonium Lead Iodide Perovskite Photovoltaics. *ACS Appl. Mater. Interfaces*, **10,** 15548-15557 (2018).
16. Joo, J., Long, S. M., Pouget, J. P., Oh, E. J., MacDiarmid, A. G., Epstein, A. J. Charge transport of the mesoscopic metallic state in partially crystalline polyanilines. *Phys. Rev. B*, **57,** 9567-9580 (1998).
17. Yoon, C. O., Reghu, M., Moses, D., Cao, Y., Heeger, A. J. Thermoelectric power of doped polyaniline near the metal-insulator transition. *Synth. Met.*, **69,** 273-274 (1995).
18. Holland, E. R., Monkman, A. P. Thermoelectric power measurements in highly conductive stretch-oriented polyaniline films. *Synth. Met.*, **74,** 75-79 (1995).